Magma fragmentation in highly explosive basaltic eruptions induced by rapid crystallisation

Fabio Arzilli[1], Giuseppe La Spina[1], Mike R. Burton[1], Margherita Polacci[1], Nolwenn Le Gall[2], Margaret E. Hartley[1], Danilo Di Genova[3], Biao Cai[4], Nghia T. Vo[5], Emily C. Bamber[1], Sara Nonni[5], Robert Atwood[5], Ed W. Llewellin[6], Heidy Mader[7] and Peter D. Lee[2]

[1]School of Earth and Environmental Sciences, University of Manchester, Manchester M139PL, UK

[2]Department of Mechanical Engineering, University College London, London, UK

[3]Institute of Non-Metallic Materials, Clausthal University of Technology, Zehntner Str. 2a, 38678 Clausthal-Zellerfeld, Germany

[4] School of Metallurgy and Materials, University of Birmingham, Birmingham B15 2TT, UK

[5]Diamond Light Source, Harwell Science and Innovation Campus, Didcot OX11 0DE, UK

[6]Department of Earth Sciences, Durham University, Durham DH1 3LE, UK

[7]School of Earth Sciences, University of Bristol, Bristol BS8 1RJ, UK

[*]Corresponding author: Dr. Fabio Arzilli

Corresponding author present affiliation: School of Earth and Environmental Sciences, The University of Manchester, Oxford Road, Manchester, M13 9PL, UK

E-mail address: fabio.arzilli@manchester.ac.uk

Phone: +393298429732; +447904104670

Basaltic eruptions are the most common form of volcanism on Earth and planetary bodies. The low viscosity of basaltic magmas inhibits fragmentation[1,2] and highly explosive activity, favouring effusive and lava-fountaining activity[3], yet highly explosive, hazardous basaltic eruptions do occur[4-8]. The processes which promote fragmentation of basaltic magma remain unclear, and are subject to debate[2,4-11]. Crystallisation during magma ascent may significantly increase magma viscosity, leading to fragmentation[11], but crystallisation in basaltic magmas has previously been thought to occur on timescales significantly longer than the minutes required for magma to ascend from a crustal storage chamber to the vent[12], particularly in the case of highly explosive eruptions. Here, we use a numerical conduit model to show that rapid ascent of magma during explosive eruption produces large undercooling. Novel *in situ* experiments reveal that undercooling drives exceptionally rapid (~minutes) crystallisation, inducing a step-change in viscosity that triggers magma fragmentation. Experimentally-produced textures are consistent with products of basaltic Plinian eruptions, supporting our conceptual model of rapid crystallisation-driven fragmentation. We apply the numerical model to investigate basaltic magma fragmentation over a wide parameter space and find that all basaltic volcanoes have the potential to produce highly explosive eruptions. The critical requirements are initial magma temperatures lower than 1100 °C in order to reach a syn-eruptive crystal content of > 30 vol.%, and thus a magma viscosity ≥ 10^5 Pa s, which our results suggest is as a physical threshold for the fragmentation of basaltic magma. Our study provides both a demonstration and explanation of the processes that drive basaltic Plinian eruptions, revealing how typically effusive basaltic volcanoes can produce unexpected highly explosive, and hazardous, eruptions[4-8,13,14]. The remarkable insights provided by novel *in situ* observations of crystallisation provide a new research frontier for studies of crystal kinetics.

In volcanic conduits, the crystallisation kinetics of an ascending magma are driven by degassing and cooling[15-16]. Plagioclase and pyroxene crystallisation are sensitive indicators of magma dynamics in volcanic conduits[12,17-20] and their kinetically controlled abundance can rapidly change magma rheology[21-22]. Our understanding of crystallisation kinetics in magmas is underpinned by *ex situ* crystallisation quench experiments. However, *ex situ* experimental approaches ubiquitously underestimate fast crystallisation kinetics in silicate melts because it is not possible to ascertain when crystals start to form, nor, how quickly they grew to the size preserved at the moment of quenching.

A frequently used model which describes crystallisation as function of time is given by an exponential law[12,16], where the rate of crystallisation is controlled by the characteristic time $\tau^{(c)}$. The smaller $\tau^{(c)}$, the faster crystals reach their equilibrium abundance. Furthermore, La Spina et al. (ref. 12) showed that, following a thermal perturbation, the new equilibrium crystal abundance is achieved in $\sim 5\tau^{(c)}$, and that $\tau^{(c)}$ for plagioclase in basaltic magmas ascending during mild lava-fountaining activity is ~1000 s.

Plagioclase growth rates increase with magma ascent rate, as cooling and decompression rates increase[23-26]. However, the characteristic times of crystal growth during fast magma ascent have not been investigated due to the inherent limitations of *ex situ* experimental approaches. In order to quantify plagioclase and pyroxene crystallisation kinetics during rapid ascent of basaltic magma, we performed, the first *in situ* 4D (3D plus time) crystallisation kinetics experiments under fast cooling rates, using fast synchrotron X-ray microtomography. Our experiments provide the first estimation of the characteristic time for plagioclase and pyroxene crystallisation in basaltic magmas during a rapid and continuous increase of undercooling (where ΔT is defined as the difference between the highest temperature at which plagioclase and pyroxene is expected to crystallise and the temperature of the magma)[17-20]. Crystallisation experiments were performed *in situ* at beamline I12-JEEP, Diamond Light Source, Harwell, UK, using a basaltic glass from the 2001 Etna eruption as the starting material (see Methods). We combined a bespoke high-temperature environmental cell[27] with fast synchrotron X-ray microtomography to image the evolution of crystallisation in real time[28] in two experiments. After 4 hours at sub-liquidus conditions (1170 °C and 1150 °C) the system was perturbed through a rapid cooling rate of 0.4 °C/s, inducing a sudden increase of undercooling (ΔT). Our results show that plagioclase crystals only grew during this final stage of rapid cooling, specifically between 1112 and 1073 °C after a dwell time of 4 hours at 1150 °C (Fig. 1) and between 1092 and 1053 °C after a dwell time of 4 hours at 1170 °C (Extended Data Fig. 1a,b,c). Plagioclase crystals grew to equilibrium abundance in less than 90 seconds (Fig.1), i.e. between two 3D scans. Following this initial burst of rapid plagioclase growth, dendritic pyroxene crystals began to nucleate heterogeneously on plagioclase and grew to their final size in the following 180 seconds (Fig. 1b,c; Extended Data Fig. 1d,e).

The large ΔT reached in a relatively short time during our *in situ* 4D crystallisation experiments produced distinctive skeletal plagioclase crystals with swallow-tail morphology and dendritic pyroxene (Fig. 2a-c), similar to the skeletal plagioclase and dendritic pyroxene crystals observed in the products of explosive basaltic Plinian eruptions[4-10], for example, Etna 122 B.C.[4,5,9,10] (Fig. 2d). Heterogeneous nucleation of pyroxene on plagioclase (Fig. 1b) is observed to occur in ~180 s during our 4D experiments. These distinctive textures are also reported in products of the Fontana Lapilli (Nicaragua)[8-10] and 1886 Tarawera (New Zealand) eruptions[4,6,7]. Therefore, all the studied examples of basaltic Plinian deposits show features that are consistent with the textures produced in our experiments. Furthermore, the signature skeletal and dendritic pyroxene is also observed in sub-Plinian eruption (Yufune 2) products of Mt. Fuji (Japan)[13].

Plagioclase crystallisation occurred at ΔT between 75 and 155 °C, whilst pyroxene crystallised at ΔT between 60 and 190 °C. This indicates that a rapid increase of ΔT (>60 °C) induces fast crystallisation. Since the equilibrium pyroxene crystal content is achieved within ~180 s, we can infer that the pyroxene characteristic time under large ΔT is < 40 s. For plagioclase, where the equilibrium crystal content is achieved within 90 s the characteristic time is < 20 s. This is two orders of magnitude less than the characteristic time found by La Spina et al. (ref. 12) for effusive and lava fountaining activities at Etna (Italy), Stromboli (Italy) and Kilauea (Hawaii), which involved much smaller ΔT (30-60 °C)[12]. The growth rate of dendritic pyroxene is $2x10^{-5}$ cm/s (Extended Data Table 1). Considering only the largest crystals, the plagioclase growth rate is $3x10^{-4}$ cm/s, while the minimum growth rate is $3x10^{-5}$ cm/s (Extended Data Table 1). These growth rates are up to two orders of magnitude higher than those estimated by previous *ex situ* experimental studies at similar ΔT in basaltic melts[23-25,29], presumably because of the inherent limitations of *ex situ* techniques.

Large undercooling can produce significant syn-eruptive microlite crystallisation during rapid magma ascent[17-20]. This increase in crystallinity dramatically increases the viscosity of the magma[2]. This process has been proposed to explain explosive basaltic Plinian eruptions, supported by evidence of high microlite contents in basaltic Plinian eruption products[4-10]. However, no mechanism for exceptionally fast crystallisation has been proposed.

Magma fragmentation in basaltic Plinian eruptions has been investigated with conduit models, where crystallisation has been assumed either to be constant[30] or at equilibrium[11]. Recent results demonstrate that disequilibrium crystallisation plays a fundamental role in magma dynamics within the conduit[12], but syn-eruptive disequilibrium crystallisation has not yet been considered for basaltic explosive volcanism[11,30].

We used the conduit model described by La Spina et al. (ref. 12, 16) to investigate the effect of our new experimentally constrained characteristic times for crystal growth with large undercooling on the ductile-brittle transition of basaltic magma. As a test case, we consider the 122 B.C. Etna basaltic Plinian eruption[4,5,31]. To model fragmentation we adopt the strain-rate criterion introduced by Papale (ref. 1):

$$\dot{\gamma} = k\frac{G_\infty}{\mu} \quad (1)$$

where $\dot{\gamma}$ is the elongational strain rate, k=0.01 is a constant, μ is the magmatic viscosity and G_∞ is the elastic modulus at infinite frequency. The other constitutive equations are reported in the

Methods section. In Figure 3 we report the calculated plagioclase undercooling, crystal content and viscosity vs depth for $\tau^{(c)} = 10$ and 1000 s. Large undercooling is produced by adiabatic expansion of exsolved volatiles, and mitigated by the latent heat of crystallisation for $\tau^{(c)} = 10$ s (Fig. 3a). In the case of fast crystal growth (i.e. $\tau^{(c)} = 10$ s) our model predicts a rapid increase in viscosity at depths below 2 km (Fig. 3c), leading to fragmentation and explosive Plinian eruption. For $\tau^{(c)} =$ 1000 s, crystal growth is slow, and viscosity stays within the fragmentation threshold. In this case, the model predicts a lava fountain-type eruption.

Having established a new model to explain basaltic Plinian eruptions, and inspired by the natural cases of strongly fragmented explosive eruptions such as Fuji[13] and Etna 2013[14], we performed a sensitivity study with our numerical model to investigate the parameter space whereby basaltic fragmentation driven by rapid crystallisation may occur. We use the Etna 122 BC eruption as a test case. We focus on the behaviour of ΔT as a function of characteristic time of crystallisation, pressure, temperature and magmatic H_2O content at the conduit inlet, conduit radius, and initial phenocryst content. A detailed description of the initial condition of the sensitivity study can be found in the Methods section. We performed each sensitivity study assuming a characteristic time of $\tau^{(c)} = 10$ s as observed in our experiments and $\tau^{(c)} = 1000$ s, as observed for Etna 2001 in mild explosive activity. We also examined $\tau^{(c)} = 1$ and 100 s for completeness.

Our model shows that undercooling is principally controlled by $\tau^{(c)}$, initial temperature and water content (Fig. 4a). ΔT at the point of fragmentation increases as initial temperature decreases (Fig. 4b), meaning that cooler magma in the chamber is most likely to produce fragmentation during ascent and eruption (Fig. 4d). This is supported by estimates of pre-eruptive temperatures obtained for the Etna and Fontana Plinian eruptions, which range between 1000 and 1060 °C[9]. Furthermore, increasing the initial total H_2O produces an increase of ΔT (Fig. 4c), because higher volatile content in the magmatic mixture leads to greater reduction in temperature through adiabatic gas expansion in the conduit. Again, this suggests that a cooling magma chamber undergoing fractional crystallisation may increase H_2O content in residual melt and produce a higher probability of an explosive eruption.

Our model results show that a higher pre-eruptive crystal content results in a greater likelihood of explosive eruptions (Fig. 4e). However, products erupted from basaltic Plinian eruptions are characterized by a small phenocryst content (<10 vol.%)[4,5,7-10,30]. Therefore, our results highlight that it is the small $\tau^{(c)}$ of syn-eruptive crystallisation that is the primary cause for an increase in the probability of magma fragmentation (Fig. 4f).

When the syn-eruptive crystal content exceeds 30 vol.%, all numerical solutions generate an explosive eruption (Fig. 4f) due to viscosity exceeding a threshold of 10^5 Pa s and triggering fragmentation (Fig. 4g). Therefore, 10^5 Pa s is a physical threshold determining a drastic change in basaltic magma rheology and eruptive style, and is most likely to be exceeded when $\tau^{(c)}$ is small (Fig. 4g). This threshold is one order of magnitude lower than previously reported for low-viscosity magmas[1,32].

Experimental and natural observations combined with a numerical model allow us to conclude that pre-eruptive temperatures <1100 °C favour the formation of highly explosive basaltic eruptions, such as Plinian volcanism, driven by fast syn-eruptive crystal growth under high undercooling. This implies that all basaltic systems on Earth have the potential to produce powerful explosive eruptions.

METHODS

Starting material. The starting material, used for our crystallisation experiments, is a trachybasalt from the lower vents of the 2001 Mt. Etna eruption[28,33]. The anhydrous, glassy starting material was obtained by melting crushed rock samples in a Pt crucible. Melting was performed in a Nabertherm® $MoSi_2$ box furnace at 1400 °C and at atmospheric pressure. The melt was left in the furnace for four hours to allow the melt to fully degas and to dissolve the crystals present. The melt was then quenched in air to glass. This procedure was repeated two times to homogenise the melt. Finally, glassy cylinders 3 mm in diameter and 4 mm in length were drilled from the synthesized glass for *in situ* 4D crystallisation experiments.

The chemical composition of the glassy starting material has been analysed with a Jeol JXA 8530 F microprobe in the facilities of the School of Earth and Environmental, Sciences, University of Manchester, UK, and are reported in Extended Data Table 2. Analyses were performed using a 15 kV accelerating voltage, 10 nA beam current and beam size of 10 µm. Standards used for calibration were albite for Na, periclase for Mg, corundum for Al, fayalite for Fe, tephroite for Mn, apatite for P, sanidine for K, wollastonite for Ca and Si and rutile for Ti. Sodium and potassium were measured first to minimize loss owing to volatilisation.

***In situ* synchrotron X-ray microtomography experiments.** The experiments were performed at the beamline I12-JEEP[34], Diamond Light Source, Harwell, UK. For these *in situ* crystallisation experiments, we used the high-temperature resistance Alice furnace[35], which allows us to control cooling at 0.05 °C/sec to 0.4 °C/sec, and the P2R in situ rig[27] for high speed rotation. The glassy cylinders were heated *in situ* in the Alice furnace up to 1250 °C for 30 minutes (Extended Data Figure 2). After the initial annealing period, crystallisation was induced by decreasing temperature from 1250 °C to 1170 °C or 1150 °C at ambient pressure, holding at the final temperature for 4 h[28] (Extended Data Figure 2). After this step, the system was perturbed by a rapid cooling at rate of 0.4

°C/s in order to investigate the rapid crystallisation in real time (Extended Data Figure 2), reaching high undercooling (up to ~200 °C) in a short time.

The experiments were performed in phase-contrast mode, setting the sample-to-detector distance at 2300 mm in order to work in the edge-detection regime[36] (Extended Data Table 3). The projections were acquired using a monochromatic X-ray beam with energy of 53 keV. In each scan, 1800 tomographic projections were acquired by the detector with equiangular steps over a full rotation angle of 180° (Extended Data Table 3). The exposure time for the acquisition of each projection was 0.05 s (Extended Data Table 3), therefore, the temporal resolution of each scan was of 90 seconds. The isotropic pixel size is 3.2 μm. The detector was a high-resolution imaging PCO edge camera with optical module 3, corresponding to a field of view of 8.0 mm × 7.0 mm. Scan acquisition started before the end of the annealing, covering the cooling period between 1250 °C and the dwell temperatures (1170 and 1150 °C), the entire duration of the dwell time and the final rapid cooling rate of 0.4 °C/s.

Image reconstruction and processing. Tomographic projections were reconstructed into 32-bit slices by using Diamond I12 in-house python codes, using the *gridrec* algorithm[37,38] (http://confluence.diamond.ac.uk/display/I12Tech/Reconstruction+scripts+for+time+series+tomography)[39,40]. The pre-processing pipeline includes centre of rotation calculation[39], zinger removal, blob removal[40], and regularisation-based ring removal[41].

The reconstructed slices were converted to 8-bit raw format and stacked using ImageJ software[42] to obtain volumes in which the isotropic voxel has an edge size of 3.2 μm. Reconstructed volumes of experiments ET1150 and ET1170 were then cropped using Avizo® software v.8.0 (FEI Visualization Sciences Group) in order to select the volume of interest (VOI) (Extended Data Table 3). In the experiment ET1150 plagioclase and pyroxene crystals nucleated and grew in a relatively large pocket of melt (Figs 1 and 2). Therefore, the VOI selected consists of a volume of melt where the rapid crystallisation of plagioclase and pyroxene occurred during the final rapid cooling rate of

0.4 °C/s. In the experiment ET1170 plagioclase and pyroxene crystals formed in narrow layers of melt (Extended Data Figure 1), during rapid continuous cooling at a rate of 0.4 °C/s.

Three-dimensional visualization (volume rendering) of the reconstructed volumes was obtained using the commercial software VGStudio 3.0 (Volume Graphics), which allowed us to make 3D textural observations of the plagioclase and pyroxene crystal morphologies (Fig. 2; Extended Data Fig. 1). Therefore, the reconstructed volume of each scan allowed us to quantify when and at which range of temperature plagioclase and pyroxene crystals were able to form.

Image segmentation and analysis of plagioclase. Segmentation is the process that allows separation of objects from the background to obtain binary volumes containing only the feature of interest. Segmentation of plagioclase crystals from the glassy matrix was performed using the semi-automatic volume segmentation[43,44] in Avizo software v. 8.0 (Extended Data Table 3). This segmentation requires manual drawing of the outlines of crystals on the 2D slices. This is repeated every 5–10 slices, depending on the size of the crystal and the complexity of their shape, along the crystal length. The crystal shape is reconstructed automatically by the software through an interpolation procedure. The advantage of this technique is that the operator can obtain the real morphology of the object of interest by visual inspection[43,44].

The reconstructed 3D images were processed and analysed with the Pore3D software library, custom-developed at Elettra[45]. The Pore3D software allowed us to quantify the number of plagioclase crystals, the volume and the maximum length of each crystal, operating directly in the 3D domain[45,46]. As we were able to obtain the 3D shape of plagioclase crystals and the real maximum axis length (L_{3D}) we could calculate the growth rate (Y_{L3D}) of plagioclase crystals (Extended Data Table 1), using the experimental duration of growth (experimental duration). The growth rate was estimated using the following equation[43]:

$$Y_{L3D} = (L_{3D}*0.5)/t_{growth}$$

where t_{growth} is the time required for crystal growth. The microtomography images give us the opportunity to measure the volume of crystals. The volumetric growth rate (Y_V) was calculated (Extended Data Table 1) using the following relationship[43]:

$$Y_V = (V*0.5)/t_{exp}$$

where V is the volume of the crystal.

Image analysis of pyroxene growth kinetics. Back-scattered electron (BSE) images were collected, using a JEOL JSM-6390LA FE-SEM at the School of Earth and Environmental Sciences, University of Manchester, Manchester, UK, in order to analyse the pyroxene morphologies and kinetics. We used an acceleration voltage of 15 kV and beam current of 10 nA. The sizes of dendritic pyroxene crystals were measured in the 2D domain, using BSE images and ImageJ software[42], as pyroxene morphologies formed during continuous cooling are difficult to resolve and analyse in the 3D domain. The pyroxene growth rate is calculated by dividing the entire length of the dendritic crystal over the duration of the pyroxene growth (Extended Data Table 1), as dendritic crystals grow in one direction.

Constitutive equations for the conduit model. In this work we use the 1D steady-state model for magma ascent described by ref. (12, 16, 47). The governing equations used in this work are reported in ref. (47). The application to a specific volcano is achieved by providing constitutive equations to describe the specific rheological, solubility, crystallisation, outgassing, and fragmentation behaviour of the system.

Following ref. (48), the viscosity of the liquid phase is modelled as:

$$\mu_l = \mu_{melt} \cdot \theta(x_c^l),$$

where μ_{melt} is the viscosity of the bubble-free, crystal-free liquid phase and θ is a factor which increases viscosity due to the presence of crystals[49].

We use an empirical relationship to estimate μ_{melt} as a function of water concentration and temperature, as in ref. (50) (based on the Vogel-Fulcher-Tammann equation):

$$\log(\mu_{melt}) = \mathrm{A} + \frac{\mathrm{B}(\mathrm{y}, x_{d_{H_2O}}^{md})}{T - \mathrm{C}(\mathrm{y}, x_{d_{H_2O}}^{md})},$$

where the viscosity μ_{melt} is in Pa s and T is the temperature in Kelvin. The parameter A is the logarithmic value of the viscosity at infinite temperature and it is assumed to be constant for all melts. The parameters B and C, instead, are functions of the melt composition y and of the dissolved water content $x_{d_{H_2O}}^{md}$. In this work, we used the composition of the average melt inclusion composition (Etna 122 B.C.) from ref. (51). Furthermore, as crystallisation proceeds, viscosity is increased according to the empirical model described in ref. (52):

$$\theta = \frac{1 + \varphi^{\delta}}{[1 - F(\varphi, \xi, \gamma)]^{B\phi^*}},$$

where

$$F = (1 - \xi) erf\left[\frac{\sqrt{\pi}}{2(1 - \xi)} \varphi(1 + \varphi^{\gamma})\right], \quad \varphi = \frac{\left(\sum_{j=1}^{n_c} x_{c_j}^{l}\right)}{\phi^*}.$$

The fitting parameters B, δ, ξ, γ and ϕ^* chosen for this work are the same used in ref. (53).

The model proposed in this work takes into account two different gas components: water and carbon dioxide. The equilibrium profile of the dissolved gas content $x_{d_i}^{md,eq}$ of component i follows the Henry's Law, i.e.

$$x_{d_i}^{md,eq} = \sigma_i \left(\frac{P_{g,i}}{\bar{P}}\right)^{\varepsilon_i},$$

where $P_{g,i} = \alpha_{g_i} P_g / \alpha_g$ is the partial pressure of the i-th gas component expressed in Pa, $\bar{P} = 1$ Pa is used to make the expression in the brackets adimensional, σ_i is the solubility coefficient and ε_i is the solubility exponent. We assume that the solubility parameter σ_i and ε_i are constant during the ascent. For this work we adopted the following parameters $\sigma_{H_2O} = 1.8911 \times 10^{-6}$; $\varepsilon_{H_2O} = 0.5257$; $\sigma_{CO_2} = 2.2154 \times 10^{-12}$; $\varepsilon_{CO_2} = 1.075$. In this work, we assume also equilibrium exsolution, which means that the dissolved volatile contents always follow the equilibrium profile.

The crystallisation model adopted here has been proposed in ref. (16). We consider the three different major crystal components erupted by Etna volcano: plagioclase, pyroxene and olivine. We assume that crystals stay coupled with the melt (i.e. no fractional crystallisation). For a better modelling of crystal nucleation and growth, we also assume that the equilibrium crystal contents are functions of temperature, pressure and dissolved water content. With these assumptions, the equilibrium mass fraction $x_{c_j}^{l,eq}$ of crystal phase j is computed using the polynomial function

$$x_{c_j}^{l,eq}(P^*,T^*,x_d^*) = \zeta_{j,1}(P^*)^2 + \zeta_{j,2}(T^*)^2 + \zeta_{j,3}(x_d^*)^2 + \zeta_{j,4}(P^*)(T^*) +$$

$$+\zeta_{j,5}(T^*)(x_d^*) + \zeta_{j,6}(x_d^*)(P^*) + \zeta_{j,7}(P^*) + \zeta_{j,8}(T^*) + \zeta_{j,9}(x_d^*) + \zeta_{j,10},$$

where P^* is the liquid pressure expressed in bars, T^* is the temperature expressed in Celsius degrees and x_d^* is the dissolved water concentration in weight percent. From $x_{c_j}^{l,eq}$, the equilibrium crystal volume fraction β_j^{eq} can be computed using the relation

$$\beta_j^{eq} = \frac{\rho_l x_{c_j}^{l,eq}}{\rho_{c_j}}.$$

The parameters $\zeta_{j,i}$ are calculated fitting the polynomial function over a large range of data obtained at different pressures, temperatures and water contents with alphaMELTS[54], a command line version of MELTS[55]. As previously, we used the average melt inclusion composition (Etna 122 B.C.) from ref. (51).

The experimental phase diagram for Etna basalt erupted during the 122 B.C. eruption[9] provides the plagioclase liquidus at different pressures and temperatures, whilst the conduit model is able to track temperature evolution within the conduit. Combining both of these data, we can estimate ΔT with respect to the plagioclase liquidus during magma ascent.

For this work, since we are interested in the highly explosive activity, we assumed no relative velocity between gas and melt. Furthermore, as we indicated in the main text, we used as fragmentation model the strain-rate criterion introduced by ref. (1).

Initial condition for the sensitivity analysis.

The range of input parameters adopted for the sensitivity analysis are the following: 140–160 MPa for the inlet pressure at 6000 m depth, 1050–1100 °C for the magma inlet temperature, 5–30 m for the radius of the conduit, 2.0–4.0 wt.% for the total water content, 0.1–2.0 wt.% for the total CO_2 content, 0–20 vol.% for the initial phenocrysts, and 1–1000 s for the characteristic time of crystallisation. Since we do not know the probability distribution of the uncertain input parameters, we have assumed a uniform distribution within the aforementioned ranges. The sensitivity analysis was performed on using the DAKOTA toolkit (Design Analysis Kit for Optimization and Terascale Applications)[56], an open-source software developed at Sandia National Laboratories that provides a flexible and extensible interface between analysis codes and iterative systems analysis methods such as uncertainty quantification, sensitivity analysis, optimization, and parameter estimation.

References

1. Papale, P. Strain-induced magma fragmentation in explosive eruptions. *Nature* **397**, 425 (1999).

2. Giordano, D. & Dingwell, D. Viscosity of hydrous Etna basalt: implications for Plinian-style basaltic eruptions. *Bulletin of Volcanology* **65**, 8-14 (2003).

3. Polacci, M., Corsaro, R. A. & Andronico, D. Coupled textural and compositional characterization of basaltic scoria: Insights into the transition from Strombolian to fire fountain activity at Mount Etna, Italy. *Geology* **34**, 201-204 (2006).

4. Houghton, B. F., Wilson, C. J. N., Del Carlo, P., Coltelli, M., Sable, J. E. & Carey, R. The influence of conduit processes on changes in style of basaltic Plinian eruptions: Tarawera 1886 and Etna 122 BC. *Journal of Volcanology and Geothermal Research* **137**, 1-14 (2004).

5. Sable, J. E., Houghton, B. F., Del Carlo, P. & Coltelli, M. Changing conditions of magma ascent and fragmentation during the Etna 122 BC basaltic Plinian eruption: Evidence from clast microtextures. *Journal of Volcanology and Geothermal Research* **158**, 333-354 (2006).

6. Houghton, B. F. & Gonnermann, H. M. Basaltic explosive volcanism: constraints from deposits and models. *Chemie der Erde-Geochemistry* **68**, 117-140 (2008).

7. Sable, J. E. Houghton, B. F., Wilson, C. J. N. & Carey, R. J. Eruption mechanisms during the climax of the Tarawera 1886 basaltic Plinian eruption inferred from microtextural characteristics of the deposits. *Studies in Volcanology: The Legacy of George Walker. Special Publications of IAVCEI* **2**, 129-154 (2009).

8. Costantini, L., Houghton, B. F. & Bonadonna, C. Constraints on eruption dynamics of basaltic explosive activity derived from chemical and microtextural study: the example of the Fontana Lapilli Plinian eruption, Nicaragua. *Journal of Volcanology and Geothermal Research* **189**, 207-224 (2010).

9. Goepfert, K. & Gardner, J. E. Influence of pre-eruptive storage conditions and volatile contents on explosive Plinian style eruptions of basic magma. *Bulletin of Volcanology* **72**, 511-521 (2010).

10. Szramek, L. A. Mafic Plinian eruptions: Is fast ascent required? *Journal of Geophysical Research: Solid Earth* **121**, 7119-7136 (2016).

11. Moitra, P., Gonnermann, H. M., Houghton, B. F. & Tiwary, C. S. Fragmentation and Plinian eruption of crystallizing basaltic magma. *Earth and Planetary Science Letters* **500**, 97-104 (2018).

12. La Spina, G., Burton, M., Vitturi, M. D. M. & Arzilli, F. Role of syn-eruptive plagioclase disequilibrium crystallisation in basaltic magma ascent dynamics. *Nature communications* **7**, 13402 (2016).

13. Suzuki, Y. & Fujii, T. Effect of syneruptive decompression path on shifting intensity in basaltic sub-Plinian eruption: Implication of microlites in Yufune-2 scoria from Fuji volcano, Japan. *Journal of Volcanology and Geothermal Research*, **198**, 158-176 (2010).

14. Andronico, D., Scollo, S. & Cristaldi, A. Unexpected hazards from tephra fallouts at Mt Etna: The 23 November 2013 lava fountain. *Journal of Volcanology and Geothermal Research*, 304, 118-125 (2015).

15. Cashman, K. & Blundy, J. Degassing and crystallisation of ascending andesite and dacite. *Philosophical Transactions of the Royal Society of London A: Mathematical, Physical and Engineering Sciences* **358**, 1487-1513 (2000).

16. La Spina, G., Burton, M., de' Michieli Vitturi, M. Temperature evolution during magma ascent in basaltic effusive eruptions: a numerical application to Stromboli volcano. *Earth Planet. Sci. Lett.* **426**, 89–100 (2015).

17. Hammer, J. E. & Rutherford, M. J. An experimental study of the kinetics of decompression induced crystallization in silicic melt. *Journal of Geophysical Research: Solid Earth* **107**, ECV-8 (2002).

18. Couch, S., Harford, C. L., Sparks, R. S. J. & Carroll, M. R. Experimental constraints on the conditions of formation of highly calcic plagioclase microlites at the Soufrire Hills Volcano, Montserrat. *Journal of Petrology* **44**,1455-1475 (2003).

19. Shea, T. & Hammer, J. E. Kinetics of cooling-and decompression-induced crystallization in hydrous mafic-intermediate magmas. *Journal of Volcanology and Geothermal research* **260**, 127-145 (2013).

20. Agostini, C., Fortunati, A., Arzilli, F., Landi, P. & Carroll, M. R. Kinetics of crystal evolution as a probe to magmatism at Stromboli (Aeolian Archipelago, Italy). *Geochimica et cosmochimica acta* **110**, 135-151 (2013).

21. Vona, A. & Romano, C. The effects of undercooling and deformation rates on the crystallization kinetics of Stromboli and Etna basalts. *Contributions to Mineralogy and Petrology* **166**, 491-509 (2013).

22. Kolzenburg, S., Giordano, D., Hess, K. U. & Dingwell, D. B. Shear Rate□Dependent Disequilibrium Rheology and Dynamics of Basalt Solidification. *Geophysical Research Letters* **45**, 6466-6475 (2018).

23. Cashman, K. V. Relationship between plagioclase crystallization and cooling rate in basaltic melts. *Contributions to Mineralogy and Petrology* **113**, 126-142 (1993).

24. Conte, A. M., Perinelli, C. & Trigila, R. Cooling kinetics experiments on different Stromboli lavas: Effects on crystal morphologies and phases composition. *Journal of Volcanology and Geothermal Research* **155**, 179-200 (2006).

25. Szramek, L., Gardner, J. E. & Hort, M. Cooling-induced crystallization of microlite crystals in two basaltic pumice clasts. *American Mineralogist* **95**, 503-509 (2010).

26. Brugger, C. R. & Hammer, J. E. Crystallization kinetics in continuous decompression experiments: implications for interpreting natural magma ascent processes. *Journal of Petrology* **51**, 1941-1965 (2010).

27. Karagadde, S., Lee, P. D., Cai, B., Fife, J. L., Azeem, M. A., Kareh, K. M., Puncreobutr, C., Tsivoulas, D., Connolley, T. & Atwood, R. C. Transgranular liquation cracking of grains in the semi-solid state. *Nature communications* **6**, 8300 (2015).

28. Polacci, M., Arzilli, F., La Spina, G., Le Gall, N., Cai, B., Hartley, M. E., Di Genova, D., Vo, N. T., Nonni, S., Atwood, R. C., Llewellin, E. W., Lee, P. D. & Burton, M. R. Crystallisation in basaltic magmas revealed via in situ 4D synchrotron X-ray microtomography. *Scientific Reports* **8**, 8377 (2018).

29. Arzilli, F., Agostini, C., Landi, P., Fortunati, A., Mancini, L. & Carroll, M. R. Plagioclase nucleation and growth kinetics in a hydrous basaltic melt by decompression experiments. *Contributions to Mineralogy and Petrology* **170**, 55 (2015).

30. Campagnola, S., Romano, C., Mastin, L. G. & Vona, A. Confort 15 model of conduit dynamics: applications to Pantelleria Green Tuff and Etna 122 BC eruptions. *Contributions to Mineralogy and Petrology* **171**, 60 (2016).

31. Coltelli, M., Del Carlo, P. & Vezzoli, L. Discovery of a Plinian basaltic eruption of Roman age at Etna volcano, Italy. *Geology* **26**, 1095-1098 (1998).

32. Namiki, A. & Manga, M. Transition between fragmentation and permeable outgassing of low viscosity magmas. *Journal of Volcanology and Geothermal Research* **169**, 48-60 (2008).

33. Corsaro, R. A., Miraglia, L. & Pompilio, M. Petrologic evidence of a complex plumbing system feeding the July-August 2001 eruption of Mt. Etna, Sicily, Italy. *B. Volcanol.* **69**, 401–421 (2007).

34. Drakopoulos, M., Connolley, T., Reinhard, C., Atwood, R., Magdysyuk, O., Vo, N., Hart, M., Connor, L., Humphreys, B., Howell, G. & Davies, S. I12: the joint engineering, environment and processing (JEEP) beamline at diamond light source. *Journal of synchrotron radiation* **22**, 828-838 (2015).

35. Azeem, M. A., Lee, P. D., Phillion, A. B., Karagadde, S., Rockett, P., Atwood, R. C., Courtois, L., Rahman, K. M. & Dye, D. Revealing dendritic pattern formation in Ni, Fe and Co alloys using synchrotron tomography. *Acta Materialia* **128**, 241-248 (2017).

36. Cloetens, P., Barrett, R., Baruchel, J., Guigay, J. P. & Schlenker, M. Phase objects in synchrotron radiation hard X-ray imaging. *J. Phys. D. Appl. Phys.* **29**, 133–46 (1996).

37. O'sullivan, J. D. A fast sinc function gridding algorithm for Fourier inversion in computer tomography. *IEEE transactions on medical imaging* **4**, 200-207 (1985).

38. Gürsoy, D., De Carlo, F., Xiao, X. & Jacobsen, C. TomoPy: a framework for the analysis of synchrotron tomographic data. *Journal of synchrotron radiation* **21**, 1188-1193 (2014).

39. Vo, N. T., Drakopoulos, M., Atwood, R. C. & Reinhard, C. Reliable method for calculating the center of rotation in parallel-beam tomography. *Opt. Express* **22**, 19078–19086 (2014).

40. Vo, N. T., Atwood, R. C. and Drakopoulos, M. Superior techniques for eliminating ring artifacts in X-ray micro-tomography. *Optics express* **26**, 28396-28412 (2018).

41. Titarenko, S., Withers, P. J. & Yagola, A. An analytical formula for ring artefact suppression in X-ray tomography. *Applied Mathematics Letters* **23**, 1489-1495 (2010).

42. Abramoff M. D., Magalhaes P. J., Ram S. J. Image processing with ImageJ. *Biophot. Int.* **11**, 36–42 (2004).

43. Arzilli, F., Mancini, L., Voltolini, M., Cicconi, M. R., Mohammadi, S., Giuli, G., Mainprice, D., Paris, E., Barou, F. & Carroll, M. R. Near-liquidus growth of feldspar spherulites in trachytic melts: 3D morphologies and implications in crystallization mechanisms. *Lithos* **216**, 93-105 (2015).

44. Arzilli, F., Polacci, M., Landi, P., Giordano, D., Baker, D. R. & Mancini, L. A novel protocol for resolving feldspar crystals in synchrotron X-ray microtomographic images of crystallized natural magmas and synthetic analogs. *American Mineralogist* **101**, 2301-2311 (2016).

45. Brun, F., Mancini, L., Kasae, P., Favretto, S., Dreossi, D. & Tromba, G. Pore3D: a software library for quantitative analysis of porous media. *Nucl. Instrum. Meth. A* **615**, 326–332 (2010).

46. Ohser, J. & Mücklich, F. Statistical analysis of microstructure in material science. Barnett V, editor. Statistics in Practice, West Sussex, England: John Wiley & Sons; (2000).

47. La Spina, G., Polacci, M., Burton, M. & de' Michieli Vitturi, M. Numerical investigation of permeability models for low viscosity magmas: application to the 2007 Stromboli effusive eruption Earth and Planetary Science Letters **473**, 279-290 (2017).

48. de' Michieli Vitturi, M., Clarke, A. B., Neri, A. & Voight, B. Transient effects of magma ascent dynamics along a geometrically variable dome-feeding conduit. *Earth Planet. Sci. Lett.* **295**, 541–553 (2010).

49. Caricchi, L., Burlini, L., Ulmer, P., Gerya, T., Vassalli, M. & Papale, P. Non-Newtonian rheology of crystal-bearing magmas and implications for magma ascent dynamics. *Earth Planet. Sci. Lett.* **264**, 402–419 (2007).

50. Giordano, D., Russell, J. K. & Dingwell, D. B. Viscosity of magmatic liquids: a model. *Earth Planet. Sci. Lett.* **271**, 123-134 (2008).

51. Del Carlo, P. & Pompilio, M. The relationship between volatile content and the eruptive style of basaltic magma: the Etna case. *Annals of Geophysics*, **47** (2004).

52. Costa, A., Caricchi, L. & Bagdassarov, N. A model for the rheology of particle-bearing suspensions and partially molten rocks. *Geochem. Geophys. Geosyst.* **10**, (2009).

53. Vona, A., Romano, C., Dingwell, D. & Giordano, D. The rheology of crystal-bearing basaltic magmas from Stromboli and Etna. *Geochim. Cosmochim. Acta* **75**, 3214–3236 (2011).

54. Smith, P. M. & Asimow, P. D. Adiabat_1ph: a new public front-end to the MELTS, pMELTS, and pHMELTS models. *Geochem. Geophys. Geosyst.* **6**, (2005).

55. Ghiorso, M. S. & Sack, R. O. Chemical mass transfer in magmatic processes IV. A revised and internally consistent thermodynamic model for the interpola-tion and extrapolation of liquid–solid equilibria in magmatic systems at elevated temperatures and pressures. *Contrib. Mineral. Petrol.* **119**, 197–212 (1995).

56. Adams, B. M., Ebeida, M. S., Eldred, M. S., Geraci, G., Jakeman, J. D., Maupin, K. A., Monschke, J. A., Swiler, L. P., Stephens, J. A., Vigil, D. M., Wildey, T. M., Bohnhoff, W. J., Dalbey, K. R., Eddy, J. P., Frye, J. R., Hooper, R. W., Hu, K. T., Hough, P. D., Khalil, M., Ridgway, E. M. & Rushdi, A. DAKOTA, A Multilevel Parallel Object-Oriented Framework for Design Optimization, Parameter Estimation, Uncertainty Quantification, and Sensitivity Analysis Version 6.6 User's Manual Tech. rep., SAND2014-4633, Tech. rep., SAND2014-4633, (2017).

Supplementary information is available in the online version of the paper.

Acknowledgements

The research leading to these results has received funding from the RCUK NERC DisEqm project (NE/N018575/1) and (NE/M013561/1). The beamtime on I12 was provided by Diamond Light Source (EE16188-1) and laboratory space by the Research Complex at Harwell.

Author Contributions

M.P., F.A., M.R.B., and P.D.L. conceived the research project. F.A., M.P., G.L.S., N.L.G., B.C., M.E.H., D.D.G., N.T.V., S.N., R.C.A., E.W.L., P.D.L. and M.R.B. contributed to the beamline experiments. F.A. collected the volcanic rocks for the starting material. D.D.G. prepared the starting material. F.A., M.P. and G.L.S performed image reconstruction. F.A. and M.P. performed image processing. F.A. performed image segmentation and analysis. G.L.S. performed simulations using the conduit model. E.C.B., F.A. and G.L.S. collected samples of Etna 122 BC Plinian eruption. E.C.B. and F.A. acquired and analysed back-scattered electron images of Etna Plinian eruption’s samples. F.A., G.L.S., M.R.B., M.P. and E.C.B. wrote the manuscript, with contributions from all other authors.

Author Information

Reprints and permissions information is available at www.nature.com/reprints. The authors declare no competing financial interests. Readers are welcome to comment on the online version of the paper. Correspondence and requests for materials should be addressed to F.A. (fabio.arzilli@manchester.ac.uk)

FIGURES

Figure 1. Crystallisation through time. Reconstructed axial slices during continuous cooling at 0.4 °C/s: (a) frame after 24 s from the onset of the cooling, in which the temperature ranges between 1144 and 1112 °C (average 1128 °C); (b) frame after 208 s, in which the temperature ranges between 1073 and 1034 °C (average 1054 °C); (c) frame after 392 s, in which the temperature ranges between 997 and 959 °C (average 978 °C). m = melt; plg = plagioclase; px = pyroxene.

Figure 2. Plagioclase crystal morphology. (a) The 3D volume rendering of sample SS1150 shows the morphology and the spatial distribution of plagioclase crystals that formed during the rapid cooling at $96<\Delta T<155$ °C. (b) 3D view of the plagioclase with swallow-tailed crystal morphology. (c) Back scattered electron image of plagioclase with swallow-tailed crystal morphology. (d) Back scattered electron image of plagioclase with swallow-tailed crystal morphology produced during the Etna 122 B.C Plinian eruption. Note heterogeneous nucleation of pyroxene around plagioclase, seen as a light-coloured halo, and similar to that seen in figure 1b.

Figure 3. Model results during magma ascent. (a) Undercooling as a function of depth, calculated for τ(c) = 10 (blue) and 1000 s (red). Cooling is driven by adiabatic expansion of gas, mitigated by latent heat of crystallisation particularly in the fast crystallising case. (b) Crystal content in vol%, demonstrating the rapid increase in crystal load when τ(c) = 10 s. (c) Magma viscosity, demonstrating that the higher crystal load produces 3-4 order of magnitude increase in viscosity, leading to fragmentation.

Figure 4. Relationships between characteristic time, initial temperature, initial H_2O content of the magma, syn-eruptive crystal content and magma viscosity and the undercooling of the system at the fragmentation level. These figures were calculated using repeated runs of the model while changing individual parameters to reveal the sensitivity of the system to each parameter. Likelihood of explosive eruption as a function of a specific parameter arises from the ratio between the number of model runs producing explosive eruptions divided by the total number of model runs used to test that parameter. Therefore, this is not a probabilistic assessment of eruption risk, but instead depends on the critical model parameters, which control when fragmentation occurs, and the calculated probabilities depend on the choice of upper and lower limits chosen for each investigated parameter. (a) Sobol index. (b) Undercooling vs magma temperature before ascent. (c) Undercooling vs the initial H_2O content of the magma (dissolved and exsolved). (d) Frequency of explosive eruptions vs magma temperature before ascent. (e) Explosion frequency vs initial phenocryst content. (f) Frequency of explosive eruptions vs syn-eruptive crystal content at the fragmentation level. (g) Frequency of explosive eruptions vs magma viscosity at the fragmentation level.

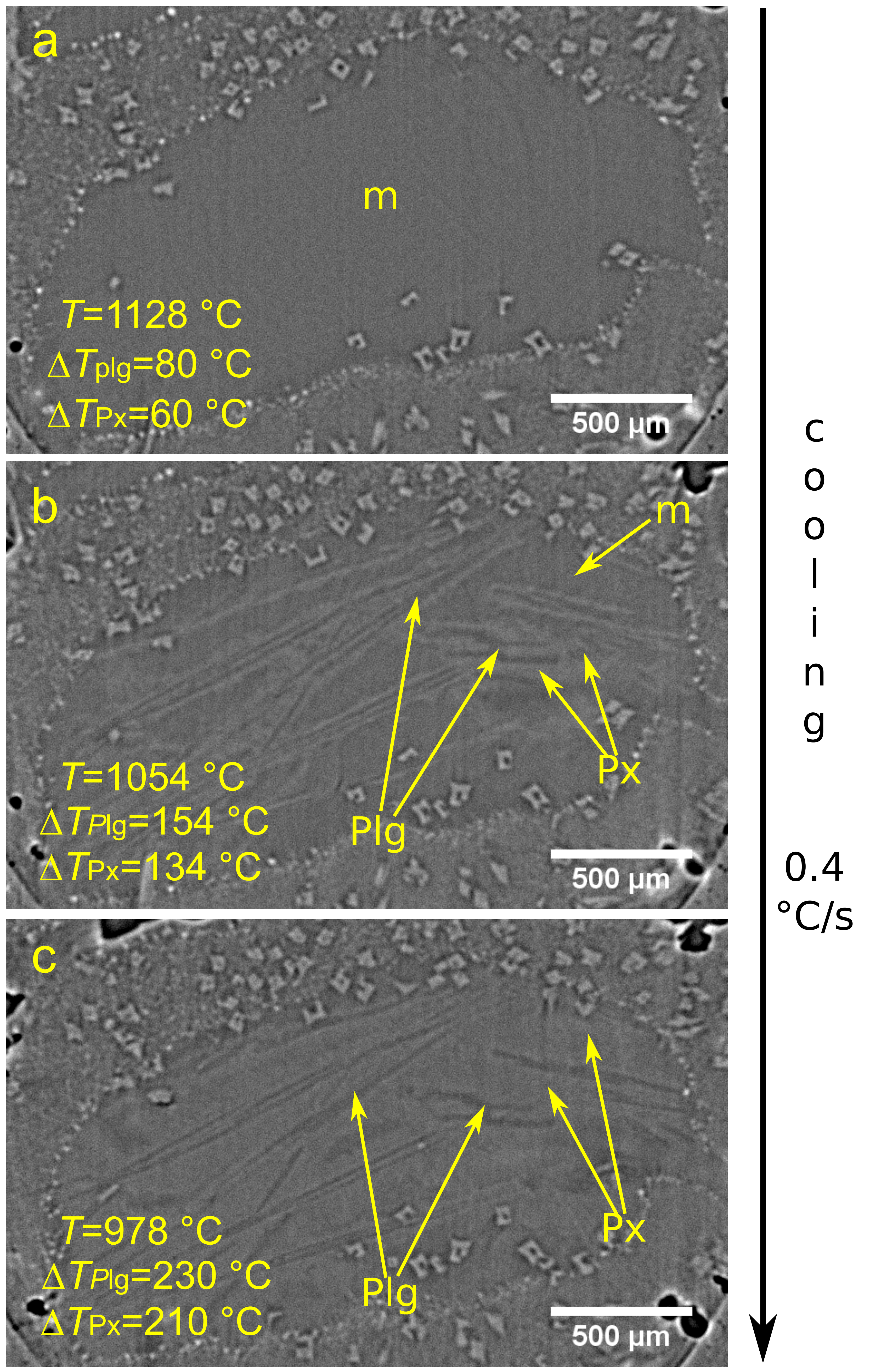

a
m
T=1128 °C
ΔTplg=80 °C
ΔTPx=60 °C
500 µm
b
m
Plg
Px
T=1054 °C
ΔTPlg=154 °C
ΔTPx=134 °C
500 µm
c
Plg
Px
T=978 °C
ΔTPlg=230 °C
ΔTPx=210 °C
500 µm
cooling
0.4 °C/s

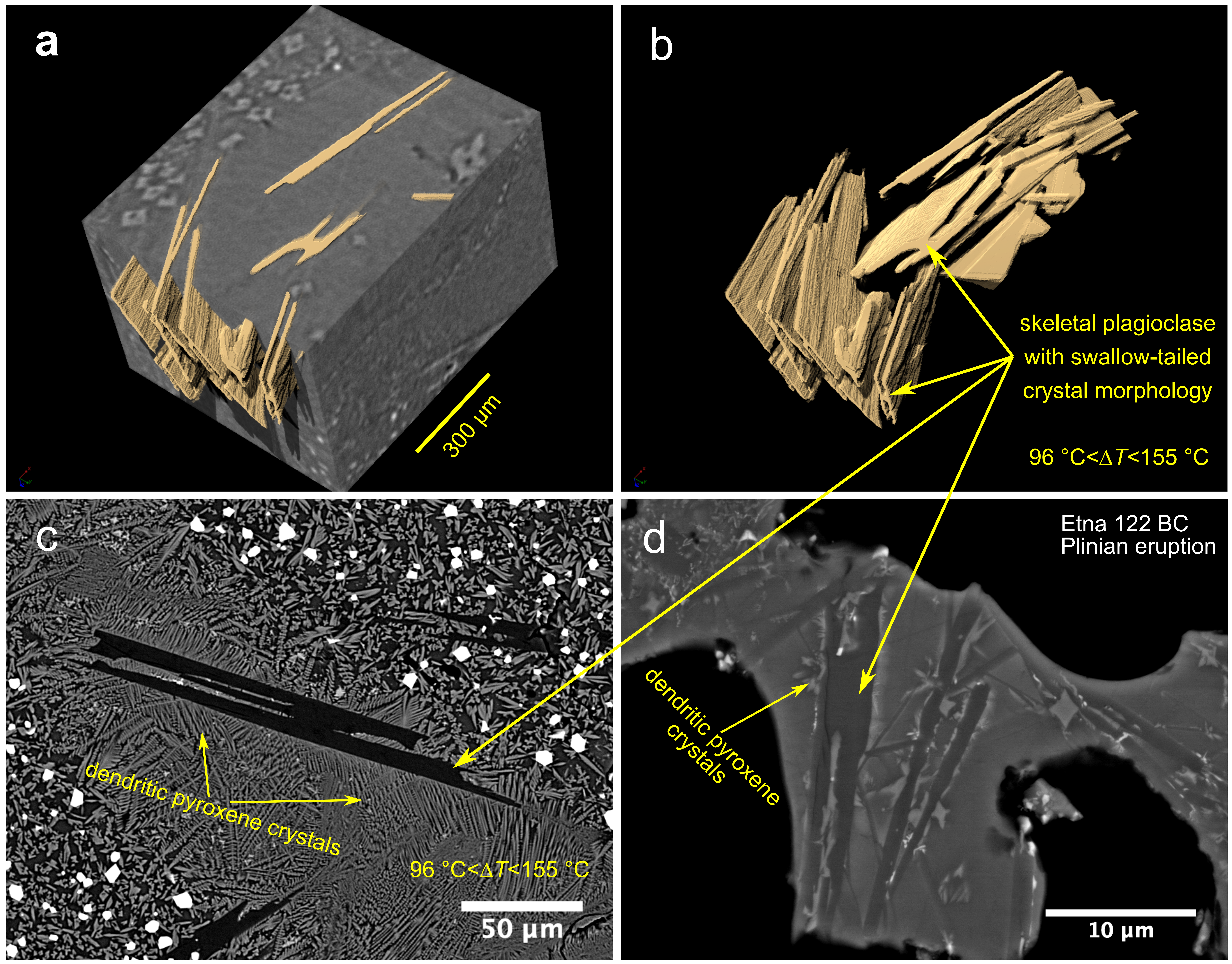
a
300 µm
b
skeletal plagioclase
with swallow-tailed
crystal morphology
96 °C<ΔT<155 °C
c
dendritic pyroxene crystals
96 °C<ΔT<155 °C
50 µm
d
Etna 122 BC
Plinian eruption
dendritic pyroxene
crystals
10 µm

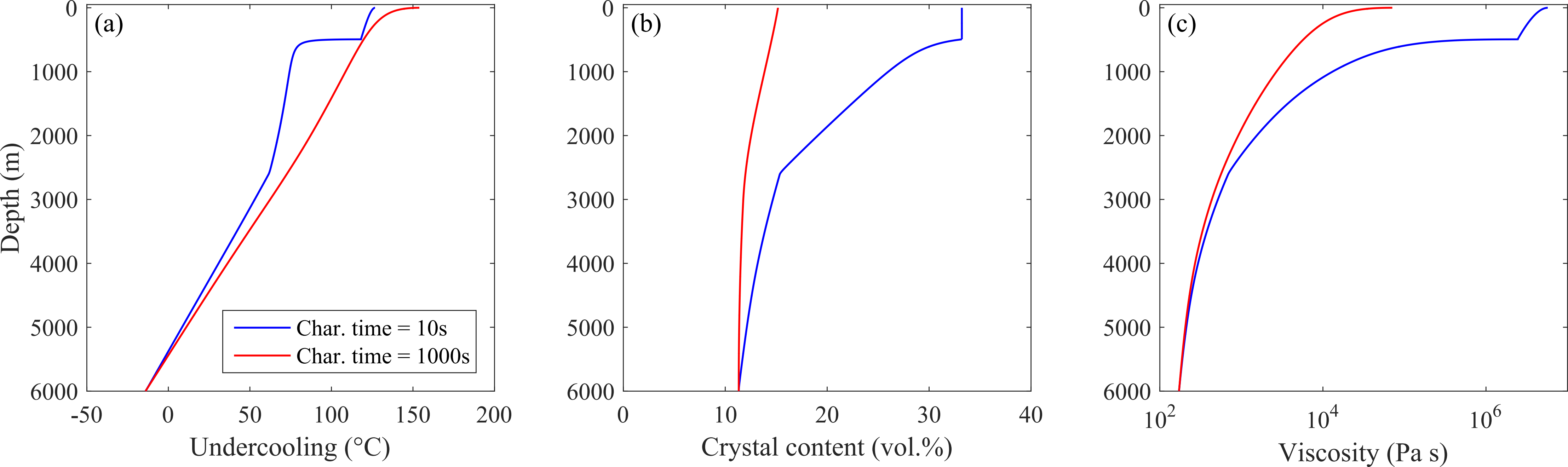

(a)
(b)
(c)
Depth (m)
0
1000
2000
3000
4000
5000
6000
-50
0
50
100
150
200
Undercooling (°C)
Char. time = 10s
Char. time = 1000s
0
10
20
30
40
Crystal content (vol.%)
10^2
10^4
10^6
Viscosity (Pa s)

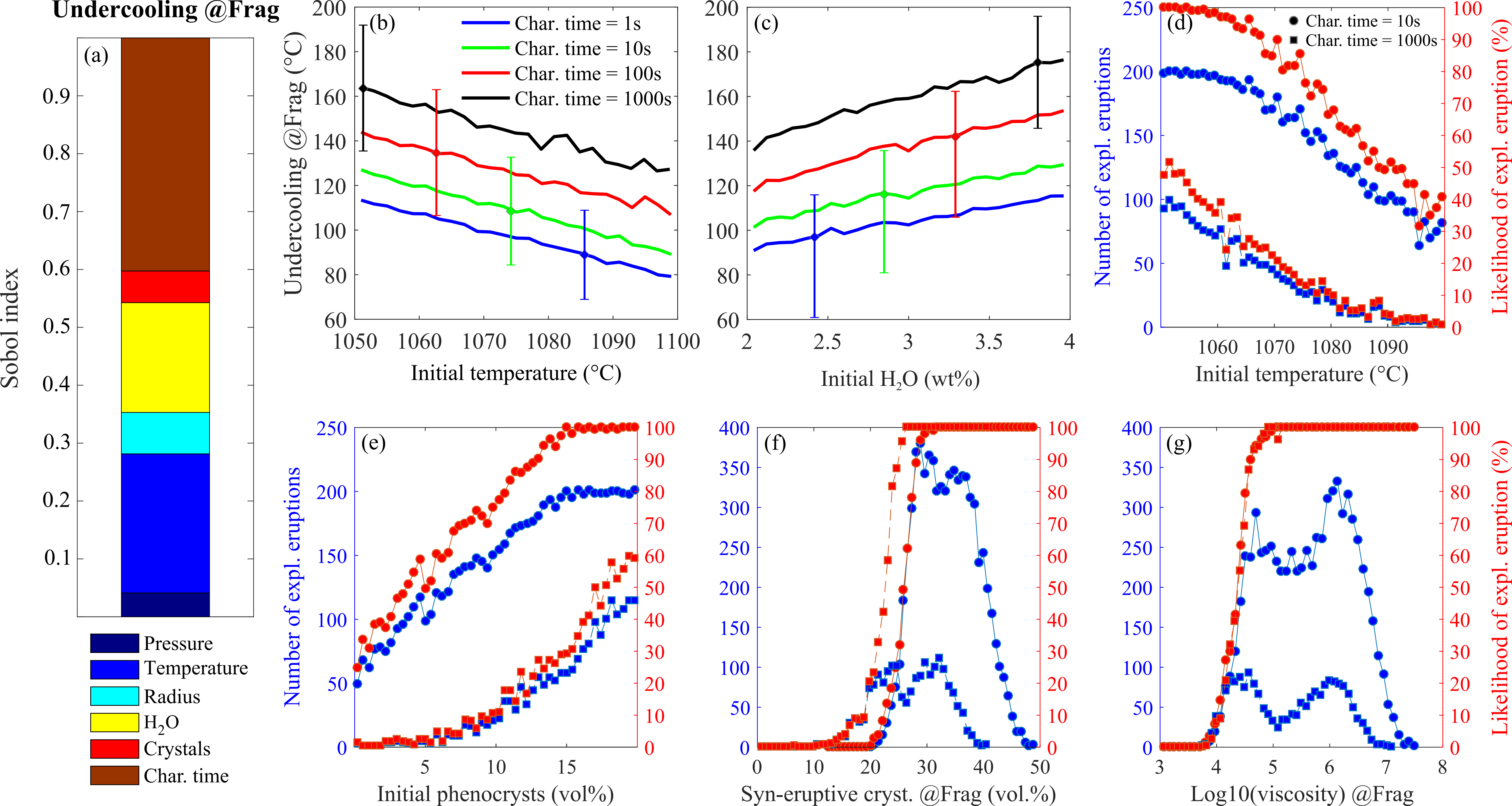

Undercooling @Frag
(a)
Sobol index
Pressure
Temperature
Radius
H_2O
Crystals
Char. time
(b)
Char. time = 1s
Char. time = 10s
Char. time = 100s
Char. time = 1000s
Undercooling @Frag (°C)
Initial temperature (°C)
(c)
Initial H_2O (wt%)
(d)
Char. time = 10s
Char. time = 1000s
Number of expl. eruptions
Likelihood of expl. eruption (%)
Initial temperature (°C)
(e)
Initial phenocrysts (vol%)
(f)
Syn-eruptive cryst. @Frag (vol.%)
(g)
Log10(viscosity) @Frag